Journal of the European Ceramic Society 41 (2021) 319–325

Contents lists available at ScienceDirect

Journal of the European Ceramic Society

journal homepage: www.elsevier.com/locate/jeurceramsoc

Original Article

Influence of orientation and ferroelectric domains on the photochemical reactivity of $La_2Ti_2O_7$

Mingyi Zhang, Paul A. Salvador, Gregory S. Rohrer *

Department of Materials Science and Engineering, Carnegie Mellon University, Pittsburgh, PA 15213, USA

ARTICLE INFO

Keywords:
Photochemistry
$La_2Ti_2O_7$
Ferroelectricity
Surface orientation

ABSTRACT

The effects of crystal orientation and ferroelectric domain structure on the photochemical reactivity of $La_2Ti_2O_7$ have been measured. Electron backscattered diffraction was used to determine the orientations of the surfaces of crystals in a ceramic specimen, piezo-force microscopy was used to determine the domain structure, and the photocathodic reduction of silver from an aqueous silver nitrate solution was used to evaluate the photochemical reactivity. The reactivity is greatest on (001) surfaces (this is the orientation of the layers in this $(110)_p$ layered perovskite structure) while surfaces perpendicular to this orientation have the least reactivity. Complex domain structures were observed within the grains, but they appeared to have no effect on the photocathodic reduction of silver, in contrast to previous observations on other ferroelectrics. $La_2Ti_2O_7$ is an example of a ferroelectric oxide in which the crystal orientation has a greater influence on the photochemical reactivity than polarization from the internal domain structure.

1. Introduction

Metal oxide semiconductors can be used to split water [1,2] and degrade organic pollutants [3,4]. Hydrogen derived from water splitting could be used as a fuel that would not increase the concentration of atmospheric CO_2. Since the discovery that water could be split using a TiO_2 photoanode and a Pt cathode [5], many other metal oxides have been shown to be able to split water [6,7]. However, none of the materials studied so far are able to produce hydrogen at rates that make it economically competitive with producing hydrogen by the conventional steam reforming of methane [8]. This has motivated studies of reaction mechanisms and sources of efficiency losses with the hope that improved catalysts can be developed [9].

One line of inquiry has been directed at determining the orientation dependence of the photochemical reactivity with the goal of designing ideal particle shapes that maximize reactivity. For example, the orientation dependence of the reactivity has been determined for rutile [10] and anatase [11] TiO_2, $BiVO_4$ [12,13], Fe_2O_3 [14], $CaTiO_3$ [15], and $SrTiO_3$ [16–18]. There are two main findings from these studies. The first is that surfaces with different crystallographic orientations can have very different reactivities. The second is that some orientations are (relatively) more photocathodic and others are more photoanodic. This provides a mechanism for charge carrier separation, making it possible to localize the reduction reaction on one surface and the oxidation reaction on another. This is thought to reduce recombination and lead to improved efficiency [19].

A second line of inquiry has been to use the positively and negatively charged domains of ferroelectrics to spatially separate the oxidation and reduction reactions and therefore improve efficiency [20]. For example, domain selective oxidation and reduction reactions have been reported on $Pb(Zr,Ti)O_3$ [21–23], $BaTiO_3$ [24], and $BiFeO_3$ [25] surfaces. Considering these two lines of inquiry, the question arises: how do the influence of crystal orientation and the presence of ferroelectric domains interact to influence reactivity? Previously, we have examined the combined influence of orientation and charged ferroelastic (rather than ferroelectric) domains, and found that orientation was the more important parameter [13,15]. We have also examined the combined influence of orientation and charged surface terminations and also found that orientation was the more important parameter [18]. However, the combined effects of ferroelectric polarization and orientation have not been explored in detail. Studies of $BaTiO_3$ [26] and $BiFeO_3$ [25] suggested that orientation is less important than the domain structure, but these studies were based on a relatively small number of observations.

Here we study the combined influence of ferroelectric domains and crystal orientation in $La_2Ti_2O_7$, a ferroelectric with the $(110)_p$ layered

* Corresponding author.
E-mail address: gr20@andrew.cmu.edu (G.S. Rohrer).

https://doi.org/10.1016/j.jeurceramsoc.2020.09.020
Received 16 July 2020; Received in revised form 3 September 2020; Accepted 8 September 2020
Available online 10 September 2020

perovskite structure [27,28]. Throughout this paper, directions in the perovskite structure will be denoted with a subscript "p". The crystal structure, illustrated in Fig. 1, has layers along [001] within which TiO_6 octahedra share corners along [100] and [012], as in the perovskite structure. Materials with this structure have the distinction of having very high Curie temperatures (T_C), which make them candidate materials for applications as high temperature piezoelectrics. Examples include, $La_2Ti_2O_7$ ($T_C \sim 1500$ °C) [29], $Sr_2Nb_2O_7$ ($T_C \sim 1330$ °C) [30], and $Pr_2Ti_2O_7$ ($T_C \sim 1750$ °C) [31]. $Sr_2Nb_2O_7$ and $La_2Ti_2O_7$ have been reported to split water under ultraviolet (UV) illumination [32]. Consistent with this observation, $La_2Ti_2O_7$ has a band gap of 3.2–3.8 eV [32–35] and band edge positions suitable to for the photocathodic reduction and photoanodic oxidation of H_2O. $La_2Ti_2O_7$ has a monoclinic structure with space group $P2_1$ (a =7.811 Å, b =5.547 Å, c =13.019 Å, β = 98.28°) and its ferroelectric polarization is along the [010] axis [31,36].

Following the observation that $La_2Ti_2O_7$ could split water, efforts have been made to modify its photochemical properties through doping and the formation of heterostructures. For example, Nashim et al. [37] have fabricated a n-$La_2Ti_2O_7$/p-$LaCrO_3$ heterostructure with an enhanced photoactivity. $La_2Ti_2O_7/In_2O_3$ heterojunction nanocomposites synthesized by Hu et al. [38] had an improved rate of hydrogen generation compared to the individual materials. Meng et al. [39] doped $La_2Ti_2O_7$ nanosheets with nitrogen and narrowed the band gap, extending the light absorption into visible light (~495 nm). Hwang et al. [33] investigated the effect of Cr and Fe doping and produced hydrogen in the presence of methanol using visible light irradiation (~420 nm).

The purpose of this paper is to describe the relative importance of crystal orientation and ferroelectric domain orientation on the photochemical properties of $La_2Ti_2O_7$. The polarization of the ferroelectric domains in $La_2Ti_2O_7$ (5 μC/cm^2) [36,40] is similar to that of $BiFeO_3$ (6 μC/cm^2), so one might assume that they would behave similarly. On the other hand, the $(110)_p$ layered perovskite structure of $La_2Ti_2O_7$ is much more anisotropic than $BiFeO_3$, so the orientation is also likely to influence reactivity. To quantify these effects, we have produced dense polycrystalline $La_2Ti_2O_7$ ceramics and measured grain orientations by electron backscatter diffraction (EBSD). The domain structure in the grains was also measured by piezo-force microscopy (PFM). After performing a photochemical marker reaction that leaves insoluble silver at the reaction site [10,41], it is possible to compare the patterns of reaction products to the grain orientation and domain structure. It has been found that the patterns of photochemically reduced silver are not correlated to the domain structure, but are correlated to the crystal orientation.

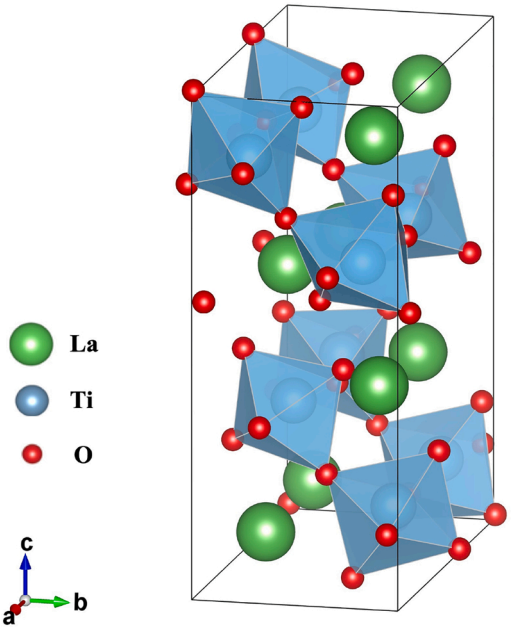

Fig. 1. Crystal structure of $La_2Ti_2O_7$ with TiO_6 octahedra shown. The polarization direction is along [010] axis.

2. Materials and methods

2.1. Sample preparation

$La_2Ti_2O_7$ powder was synthesized using a molten salt method [42]. Reagent-grade La_2O_3 (99.99 %, Alfa Aesar) and TiO_2 (99.9 %, CERAC) were mixed with a 1:2 ratio in deionized water. A salt with 50 mol % NaCl (Fisher) and 50 mol % KCl (Alfa Aesar) was then added to the mixture, constituting 50 wt % of the total reaction mixture. Then the mixture was ball-milled overnight in a plastic bottle with yttria stabilized zirconia as the grinding media. After ball milling, the mixture was dried in air at 80 °C and then heated to 1150 °C for 6 h in air in an alumina crucible. The cooled mass was washed with deionized water until the Powder X-ray diffraction (XRD) pattern showed that it was single phase $La_2Ti_2O_7$ (see Fig. S1).

Polycrystalline ceramics were prepared from the $La_2Ti_2O_7$ powder. Disk-shaped samples were formed by pressing the powders in a die, with a few drops of PVA as binder, using 130 MPa of pressure from a hydraulic press. The resulting disks had a diameter of 1 cm and a thickness of 3 mm. The samples were then put in an alumina crucible with some excess powder to insure that the pellet did not contact the crucible. The samples were calcined at 900 °C for 8 h, sintered at 1350 °C for 10 h, and coarsened at 1550 °C for 3 h. A flat surface was achieved by grinding with 600, 800, and 1200 grit silicon carbide abrasive papers (Buehler), and polishing with a series of diamond suspensions (Buehler) with a final suspension of 0.05 μm. The polished samples were then annealed at 1300 °C for 6 h to repair polishing damage and thermally etch the grain boundaries. After annealing, the microstructure consisted of randomly oriented plate-shaped grains with apparent grain diameters in the two-dimensional section plane ranging from 2 to 50 μm. The large range of apparent grain sizes arises from differently oriented sections through the anisotropically shaped grains. Finally, XRD was used to verify that the sample remained single phase $La_2Ti_2O_7$.

2.2. Characterization

EBSD was used to measure the orientations of the crystals at the surface of the $La_2Ti_2O_7$ ceramic with a FEI Quanta 200 scanning electron microscope (SEM) operated in low vacuum mode. EBSD patterns were recorded with a step size of ~ 0.5 μm and indexed by the TSL orientation imaging microscopy (OIM) software using the $P2_1$ monoclinic $Pr_2Ti_2O_7$ structure as a reference [35], but with the lattice parameter adjusted to $La_2Ti_2O_7$ (a =7.8114 Å, b =5.5474 Å, c =13.0185 Å, β = 98.719°). The data was then processed in OIM Analysis Software. A grain dilation clean-up was applied using a 5° tolerance angle, a 10-pixel minimum grain size and a multiple row requirement. All of the orientations segmented to be part of a single grain were then used to determine a single average orientation for each grain.

A NT-MDT Solver NEXT atomic force microscope (AFM) was used to record topographic and PFM images. Images were formed using conductive probes with a Pt/Ir coating from Nanoworld (ARROW-EFM). An AC bias of 4 V with a frequency of approximately 350 kHz was used where the first contact resonance was observed. Because of the sample's low electronic conductivity, it had to be thinned to less than 1.5 mm in thickness and copper contacts had to be applied to the top and bottom of the sample. The sample was cleaned with acetone before and after the PFM measurements. The samples were then used to reduce Ag^+ with photochemical marker reactions. An O-ring was placed on the top of the sample, and a few drops of 0.115 M $AgNO_3$ (Acros) aqueous solution

were added to fill the O-ring, and a quartz slip was placed on the top to seal the liquid. The sample was then illuminated by a mercury lamp (Newport) operated at 150 W for 20 min. After illumination, the sample was rinsed in DI water and dried with a stream from an aero duster (Miller-Stephenson). The locations of silver deposits were determined using an FEI Quanta 200 SEM with a 20 kV beam with a spot size of 4. Before any subsequent reaction, the sample was wiped with cotton swabs and ultrasonically cleaned in methanol and acetone. SEM was used to make sure the silver deposits on the surfaces had been removed. It was not always possible to remove all of the silver that accumulated at the bottoms of pores or grain boundary grooves; data from these regions were not interpreted and did not influence the results.

3. Results

Fig. 2(a) shows a SEM image of the surface after the photodeposition of silver. For comparison, an EBSD orientation map of the same region is shown in Fig. 2(b). To make it easier to find the same grains in the two images, six grains are surrounded by thick white lines. Note that in this two-dimensional section, some grains are elongated while others are more equiaxed. This results from the fact that the grains are relatively plate-shaped, with large (001) faces; sections parallel to (001) appear more equiaxed (red colored grains in Fig. 2(b)) and perpendicular sections appear elongated. Also, within some grains, two distinct colors appear that correspond to two different orientations. Because the local structure within the *a-b* planes is similar to perovskite, the [100] and [010] directions are sometimes incorrectly assigned by the indexing software. In these cases, we assumed the majority assignment was correct. The OIM Analysis Software assigns a 'confidence index' (CI) to each grain orientation and it was assumed that the orientations of grains with a CI $\geq$ 0.1 are correct. A map showing the CI of each grain is illustrated in Fig. S2.

The SEM image in Fig. 2(a) does not have sufficient resolution to determine the amount of reduced silver. To illustrate this, the image in Fig. S3 shows a higher resolution image of the region around the large [001] oriented (red) grain in the upper left-hand quadrant of Fig. 1 (this grain is labeled with an asterisk). High densities of small particles of reduced silver, especially at steps, that are invisible in Fig. 2(a), are clearly imaged in Fig. S3. To quantitatively determine the amount of silver on each grain, the number of silver deposits was counted on high resolution images (see Fig. 3) using the linear intercept method; several test lines are plotted on each grain and we count the number of deposits intercepted by each line. The average number of intercepts from all lines on a single grain is taken as the number of deposits on each grain. The data was then discretized into two categories: low reactivity (average deposits <5) or high reactivity (average deposits >5). Grains with high reactivity usually have a relatively dense uniform coverage of silver deposits. Grains with low reactivity usually have an inhomogeneous silver coverage with a few large deposits on part of the surface. While the reason for this difference is not known, one might speculate that the many particles on the high reactivity grains have limited growth because they compete for silver cations in the vicinity. Examples of high and low reactivity grains are shown in Fig. 3. Note that the orientation determined by EBSD is the average grain orientation with respect to the macroscopic surface orientation. The surfaces of the grains are actually curved, so the local orientation is not always the same as the macroscopic grain orientation and this accounts for the local variations in the amount of silver. The rationale for discretizing the results into only two categories is to avoid some of the uncertainties associated with orientation measurement and local surface curvature.

To determine the orientation dependence of silver reduction, the numbers of silver deposits were measured on about 90 grains. Fig. 4 summarize the results, where the orientations of the high and low reactivity grains are plotted in Fig. 4(a) and 4(b), respectively. High-reactivity grains appear to be clustered near (001), and the number of these grains decreases with inclination from (001). The low reactivity grains have an approximately opposite distribution. There are no low reactivity grains within 30° of (001), and an increasing number of them are found further from the (001) orientation. Note that [010] is the polar axis and there is no evidence that this is a high-reactivity orientation.

The distributions of high and low reactivity orientations in Fig. 4 suggest that the results can be discriminated by a single variable, the inclination from the (001) orientation. This is similar to the method used by Munprom et al. [13] to understand the results from monoclinic $BiVO_4$. Here, the angles of inclination of the grains from (001) are classified in bins that are 10° wide. By analyzing a large number of randomly generated orientations, we can determine the fraction of observations that should be found in each bin, if the grains were randomly oriented. The fraction of the observations found in each bin, divided by the fraction expected in a random distribution, quantifies the population in units of multiples of a random distribution (MRD), as illustrated in Fig. 5. The data for this calculation are shown in Table S1. These results clearly show low reactivity orientations occur at a frequency greater than random for grains inclined by more than 60° from (001). Similarly, high reactivity orientations occur with a greater than random frequency within 30° of (001) and no low reactivity grains are found in this orientation domain. Note that correlating the relative reactivity to a single orientation parameter (the inclination from (001)) ameliorates

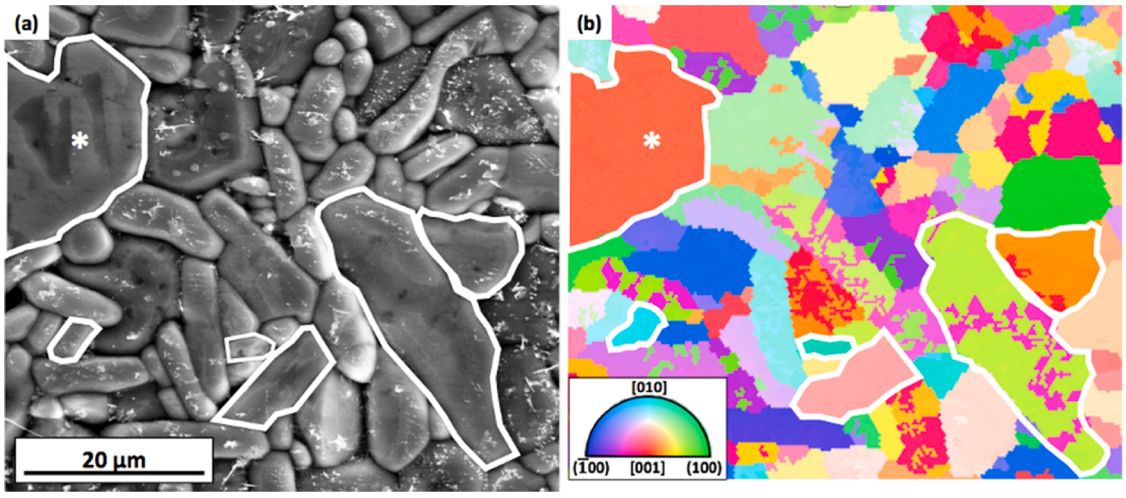

Fig. 2. (a) SE image after silver reduction. (b) Orientation map of the same area with a color key at bottom left. The field of view is about 50 µm × 60 µm. Six grains have been outlined to illustrate the correspondence between the two images.

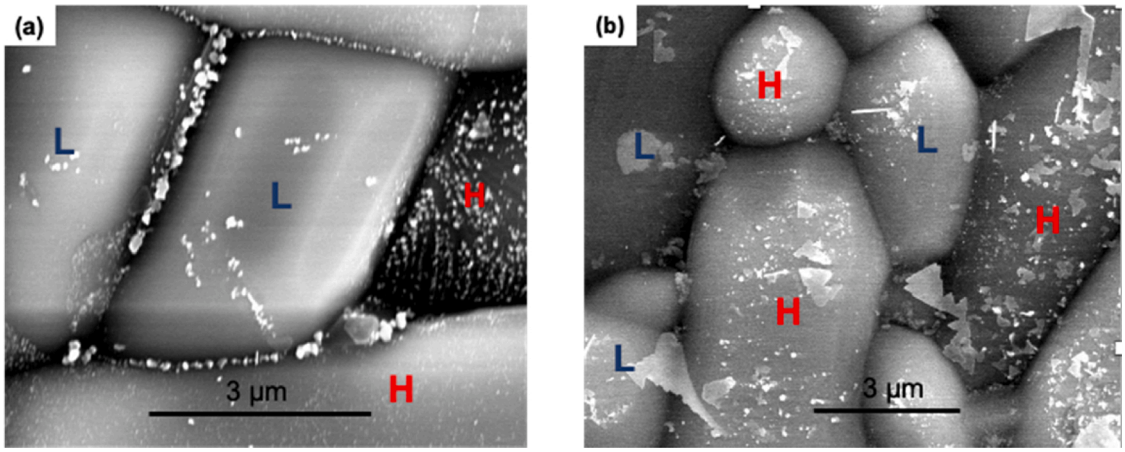

Fig. 3. SEM images of $La_2Ti_2O_7$ surfaces after the photochemical reduction of silver. High-reactivity grains are labeled with "H" while low-reactivity grains are labeled with "L".

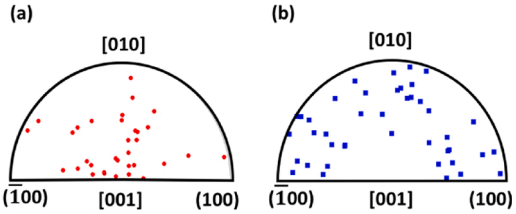

Fig. 4. Orientations of $La_2Ti_2O_7$ grains with high reactivity and low reactivity are labeled in (a) and (b), respectively. Each point corresponds to a grain and the points are plotted in the standard stereographic projection for monoclinic crystals.

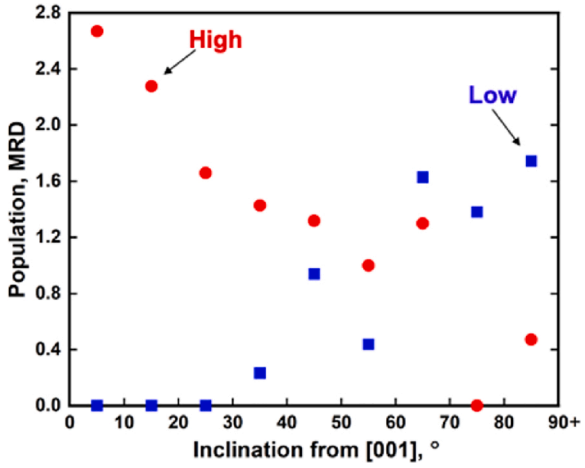

Fig. 5. The orientation distribution of grains with high reactivity (red circles) and low reactivity (blue squares) for the photochemical reduction of silver. The units are multiples of a random distribution (MRD).

problems stemming from the difficulty of distinguishing the [100] and [010] axes from the EBSD patterns.

To investigate whether ferroelectric domains influenced local reactivity, PFM was used to image grains whose orientation and relative reactivity were already measured. Out-of-plane PFM amplitude and phase images from the same grain are shown in Fig. 6(a) and (b), respectively. The amplitude image in Fig. 6(a) shows clear bright/dark contrast, indicative of domains with complex shapes. The PFM phase image in Fig. 6(b) shows strong white/black contrast on the two sides of the boundary, indicating that this is a 180° domain boundary, consistent

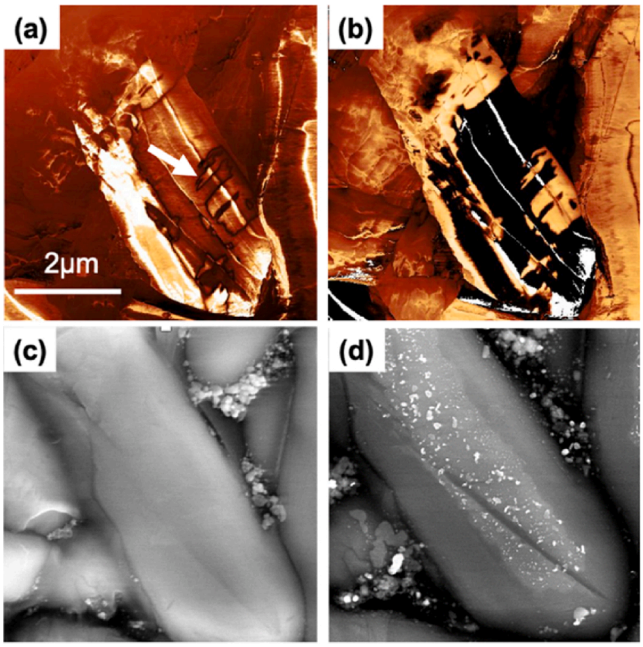

Fig. 6. A $La_2Ti_2O_7$ grain imaged with different modalities. (a) a PFM out-of-plane amplitude image. (b) a PFM out-of-plane phase image. A meandering black line in (a), marked by the arrow, corresponds to a change from light to dark contrast in the phase image. The dark (light) contrast corresponds to regions with -180° (0°) phase shift. (c & d) SEM images of the grain before (c) and after (d) photochemical silver reduction.

with our expectation for $La_2Ti_2O_7$ that domains that have polarization vectors of identical strength and opposite directions along [0 ± 10] [30,36]. This particular grain was oriented 30.1° from the polar [010] axis. While this is not very close to the polar axis, our previous work indicates that there should still be a measurable polarization (though lower than along the polar axis) normal to the surface, consistent with the PFM observations [43]. The meandering structure of the domain wall is similar to that observed in single crystals, even though the feature size is smaller in the grains of the polycrystal [36]. The domains observed in $La_2Ti_2O_7$ thin films are usually smaller than 1 μm and do not have the same meandering structure [44,45].

SEM images of the same grain shown in the PFM images are shown in Fig. 6(c) and (d), before and after photochemical silver reduction, respectively. The brightest contrast in Fig. 6(d) corresponds to silver deposits. The silver deposition is non-uniform; in this case it

accumulates mainly on the central part of the grain and in the grain boundary grooves (silver in the grooved regions is not counted). Note that the grain surface is curved because of the grain boundary grooves. The central part is flat and has the macroscopic orientation measured by EBSD, while the periphery slopes downward at an angle of approximately 10° (See AFM data in Fig. S4). In other words, the periphery of the grain has a different surface orientation and, therefore, a different reactivity. More importantly, the patterns of deposited Ag in Fig. 6(d) do not correlate with the patterns of PFM contrast. An example of another grain exhibiting a similar irregular domain shape is illustrated in Fig. S5. Ferroelectric domains in this ceramic sample have sizes as large as several micrometers. The absence of a correlation between the deposited silver and PFM contrast contradicts prior studies of ferroelectrics including $BaTiO_3$ [26], $Pb(Zr,Ti)O_3$ [23], and $BiFeO_3$ [25], in which domain selective reactivity was routinely observed.

Fig. 7(a) and (b) show an example of the reactivity and domain structure of a grain that is closer to the (010) orientation. In this case, the grain normal is inclined by 17.6° from the polar axis. Positive domains, which have bright contrast, are marked with a "+" and negative domains, which have dark contrast, are marked with a "-". In contrast with the surrounding grains, the grain near (010) reduces a very small amount of silver (see Fig. 7(a)), regardless of which domain is considered. Therefore, the domain structure has no observable influence on the reduction of silver (or absence thereof).

4. Discussion

The $La_2Ti_2O_7$ structure is anisotropic, being made up of two-dimensional slabs of the perovskite structure (with four $LaTiO_3$ perovskite layers) truncated along the [110] cubic perovskite direction (referred to as $[110]_p$). These slabs are layered parallel to the $La_2Ti_2O_7$ (001) planes, with excess oxygen (O_2) in the interlayer space between the slabs (and a concomitant relaxation of La into the region between the slabs). Hwang et al. [46] and Bruyer et al. [47] have calculated the electronic structure of $La_2Ti_2O_7$ and found that it has a direct band gap. Because materials that have direct band gaps absorb light efficiently, they suggested that this is one of the reasons it is a good water splitting catalyst. Hwang et al. [46] also suggested that the photocatalytic properties benefitted from the energetic separation of the empty Ti 3d levels, near the conduction band edge, from the empty La 4f levels, which might act as trap states.

Takata et al. [48] suggested that it was the layer structure that was responsible for the remarkable photocatalytic properties of $La_2Ti_2O_7$. Specifically, they suggested that the layers between the $[110]_p$ oriented slabs provided additional active sites for the oxidation of water. If this were so, one would expect the orientations perpendicular to the [001] direction to appear active for oxidation. While we did not study the oxidation half of the reaction, we do know that these orientations are not active for reduction. When we compare the current results to the orientation dependent reactivity of other titanates with the perovskite and perovskite-related structures, there is little similarity, suggesting that the anisotropic layered structure influences the properties more than the local structural similarities with the perovskite structure. For example, to a first approximation, the (001) surface is structurally comparable to the $(110)_p$ surface (the similarity depends specifically on which chemical plane is chosen). The results here show that for $La_2Ti_2O_7$, the photocathodic reaction occurs preferentially on the (001) surface, but in the perovskites $BaTiO_3$ [24], $SrTiO_3$ [18], and $CaTiO_3$ [15], the comparable $(110)_p$ orientation has the lowest photocathodic reactivity.

The atomic structure of $La_2Ti_2O_7$ surfaces has not, to our knowledge, been studied. The present study found that the surfaces are not faceted. However, for surfaces orientated near (001), a terrace and step structure was observed and this is consistent with previous studies [49,50].

Calculations of the band structure reported by Bruyer et al. [47] indicate that the layered structure leads to significant differences in the band edge positions perpendicular and parallel to the layers. Specifically, they show that the conduction band edge in the [001] direction is about 0.3 eV lower in energy than the conduction band energy in the [010] direction (and the band gap differs by a similar amount). A schematic energy level diagram, illustrating the relative energies of the band edges perpendicular to the (001) and (010) planes, in the flat band condition, is illustrated in Fig. 8. Based on this energy difference, there is a thermodynamic driving force for electrons, which promote the photocathodic reaction, to migrate toward the (001) surface; this is consistent with the observation that the (001) surface has the maximum photocathodic reactivity.

One aspect of the findings that is surprising is that the reactivity appears to be unaffected by the presence of ferroelectric domains, unlike nearly all of the previous ferroelectric compounds studied. One exception is that a previous study of $Sr_2Nb_2O_7$ (which is isostructural with $La_2Ti_2O_7$) also showed no clear evidence for spatially selective reactivity arising from ferroelectric domains [24]. However, that study was not conclusive because it was not possible to image domains to verify their existence and shape. Here, we can visualize the structure of the domains and see that silver is not deposited in patterns related to the domain structure. The most likely reason for this is that the surface band bending originating from the surface charge of the ferroelectric domains is not large enough to overcome the intrinsic difference in the band edge positions at different surfaces. Based on the 0.3 eV difference in the band edge positions calculated by Bruyer et al. [47], the ferroelectric domains on the (010) surface would have to bend the conduction band downward from its flat band position by at least this amount before the (010) surface could compete with the (001) surface for electrons. In comparison, the energy of the conduction band in the rhombohedral phase of $BiFeO_3$, which does show domain specific reactivity and has a similar ferroelectric polarization to $La_2Ti_2O_7$, does not depend as strongly on

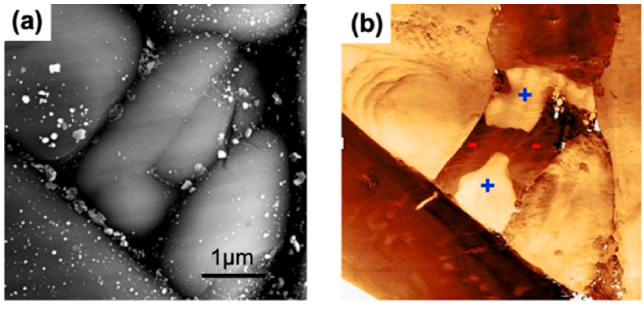

Fig. 7. (a) SE image of a surface after photochemical silver reduction. The surface orientation of the grain in the middle is 17.6° from (010). (b) PFM out-of-plane image of the same area on sample. Positive domains are labeled with "+" while negative domains are labeled with "-".

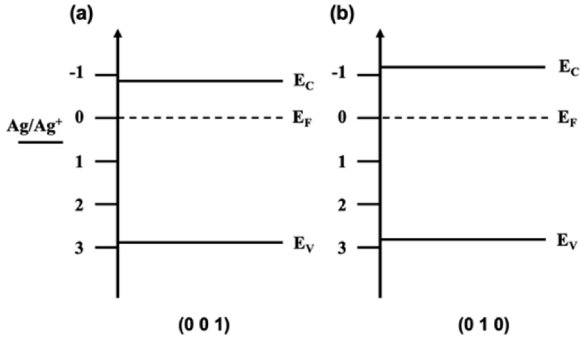

Fig. 8. Schematic energy level diagram at the $La_2Ti_2O_7$/solution interface for a (001) oriented grain (a) and a (010) oriented grain (b), assuming the flat band condition. The energy scale is in Volts. E_V, E_F, and E_C are the valence band edge, the Fermi level, and the conduction band edge, respectively.

orientation [51–53]. In other words, it is plausible that the more isotropic electronic structure of $BiFeO_3$ makes it possible to observe domain selective reduction of Ag while the anisotropic electronic structure of $La_2Ti_2O_7$ overwhelms the effects of the domains.

On the other hand, it is also plausible that a difference in the band edge positions of 0.3 eV could be overcome by band bending arising from the domain polarization. Apostol et al. [54] used XPS to determine a binding energy shift of about 1 eV between the positive and negative domains on $Pb(Zr,Ti)O_3$ surfaces and Höfer et al. [55] used photoemission electron microscopy to determine an energy difference of 1.3 V between the positive and negative domains on $BaTiO_3$ surfaces. However, these measurements were in vacuum and screening in an aqueous solution by the chemisorption of water (the conditions of our experiments) is expected to significantly reduce these values. For example, in the ambient atmosphere, Morris et al. [56] measured the band bending in $BaTiO_3$ to be in the range of 0.3–0.5 eV during illumination. Furthermore, some amount of this band bending would occur on the neutral surface and the fraction that stems from the ferroelectric polarization is not known. The exact amount of band bending on $La_2Ti_2O_7$ will depend on the orientation, the surface composition, and the reaction environment. Although accurate information about the band edge positions is currently unavailable, the observations are consistent with the idea that the anisotropy of the electronic structure is more influential than the charge associated with the ferroelectric domains.

5. Conclusion

Measurements of the orientation dependence of the reactivity of $La_2Ti_2O_7$ show that the photocathodic reduction of silver is favored on the (001) surface while perpendicular surfaces reduce much less silver. This result is consistent with what is known about the anisotropy of the electronic structure, which favors the transport of electrons to the (001) surface. Ferroelectric domains on the surface were also characterized by PFM. The domains were found to have irregular shapes and there was no correlation between the pattern of silver reduction and the domain shape. The results indicated that the ferroelectric polarization of $La_2Ti_2O_7$ does not alter the reactivity enough to overcome the influence of the anisotropic crystal structure.

Declaration of Competing Interest

The authors report no declarations of interest.

Acknowledgements

This work was supported by the National Science Foundation [grant numbers DMR 1609369 and DMR 2016267] and the authors acknowledge the use of Materials Characterization Facility at Carnegie Mellon University [grant number MCF-677785].

Appendix A. Supplementary data

Supplementary material related to this article can be found, in the online version, at doi:https://doi.org/10.1016/j.jeurceramsoc.2020.09.020.

References

[1] Y. Qu, X. Duan, Progress, challenge and perspective of heterogeneous photocatalysts, Chem. Soc. Rev. 42 (2013) 2568–2580, https://doi.org/10.1039/C2CS35355E.
[2] Z. Wang, C. Li, K. Domen, Recent developments in heterogeneous photocatalysts for solar-driven overall water splitting, Chem. Soc. Rev. 48 (2019) 2109–2125, https://doi.org/10.1039/C8CS00542G.
[3] M. Gong, S. Xiao, X. Yu, C. Dong, J. Ji, D. Zhang, M. Xing, Research progress of photocatalytic sterilization over semiconductors, RSC Adv. 9 (2019) 19278–19284, https://doi.org/10.1039/C9RA01826C.
[4] J. Luo, S. Zhang, M. Sun, L. Yang, S. Luo, J.C. Crittenden, A critical review on energy conversion and environmental remediation of photocatalysts with remodeling crystal lattice, surface, and interface, ACS Nano 13 (2019) 9811–9840, https://doi.org/10.1021/acsnano.9b03649.
[5] A. Fujishima, K. Honda, Electrochemical photolysis of water at a semiconductor electrode, Nature 238 (1972) 37+, https://doi.org/10.1038/238037a0.
[6] F.E. Osterloh, Inorganic materials as catalysts for photochemical splitting of water, Chem. Mater. 20 (2008) 35–54, https://doi.org/10.1021/cm7024203.
[7] F.E. Osterloh, Inorganic nanostructures for photoelectrochemical and photocatalytic water splitting, Chem. Soc. Rev. 42 (2013) 2294–2320, https://doi.org/10.1039/C2CS35266D.
[8] B.A. Pinaud, J.D. Benck, L.C. Seitz, A.J. Forman, Z. Chen, T.G. Deutsch, B.D. James, K.N. Baum, G.N. Baum, S. Ardo, H. Wang, E. Miller, T.F. Jaramillo, Technical and economic feasibility of centralized facilities for solar hydrogen production via photocatalysis and photoelectrochemistry, Energy Environ. Sci. 6 (2013) 1983–2002, https://doi.org/10.1039/C3EE40831K.
[9] T. Hisatomi, K. Domen, Reaction systems for solar hydrogen production via water splitting with particulate semiconductor photocatalysts, Nat. Catal. 2 (2019) 387–399, https://doi.org/10.1038/s41929-019-0242-6.
[10] J.B. Lowekamp, G.S. Rohrer, P.A. Morris Hotsenpiller, J.D. Bolt, W.E. Farneth, Anisotropic photochemical reactivity of bulk TiO_2 crystals, J. Phys. Chem. B 102 (1998) 7323–7327, https://doi.org/10.1021/jp982721e.
[11] T. Ohno, K. Sarukawa, M. Matsumura, Crystal faces of rutile and anatase TiO_2 particles and their roles in photocatalytic reactions, New J. Chem. 26 (2002) 1167–1170, https://doi.org/10.1039/B202140D.
[12] R. Li, F. Zhang, D. Wang, J. Yang, M. Li, J. Zhu, X. Zhou, H. Han, C. Li, Spatial separation of photogenerated electrons and holes among {010} and {110} crystal facets of BiVO4, Nat. Commun. 4 (2013), https://doi.org/10.1038/ncomms2401.
[13] R. Munprom, P.A. Salvador, G.S. Rohrer, The orientation dependence of the photochemical reactivity of $BiVO_4$, J. Mater. Chem. A 3 (2015) 2370–2377, https://doi.org/10.1039/c4ta06045h.
[14] Y. Zhu, A.M. Schultz, G.S. Rohrer, P.A. Salvador, The orientation dependence of the photochemical activity of α-Fe_2O_3, J. Am. Ceram. Soc. 99 (2016) 2428–2435, https://doi.org/10.1111/jace.14201.
[15] K.E. Zitello, P.A. Salvador, G.S. Rohrer, Influence of surface orientation on the photochemical reactivity of $CaTiO_3$, J. Am. Ceram. Soc. 103 (2020) 4498–4506, https://doi.org/10.1111/jace.17107.
[16] J.L. Giocondi, P.A. Salvador, G.S. Rohrer, The origin of photochemical anisotropy in $SrTiO_3$, Top. Catal. 44 (2007) 529–533, https://doi.org/10.1007/s11244-006-0101-y.
[17] L. Mu, Y. Zhao, A. Li, S. Wang, Z. Wang, J. Yang, Y. Wang, T. Liu, R. Chen, J. Zhu, F. Fan, R. Li, C. Li, Enhancing charge separation on high symmetry $SrTiO_3$ exposed with anisotropic facets for photocatalytic water splitting, Energy Environ. Sci. 9 (2016) 2463–2469, https://doi.org/10.1039/c6ee00526h.
[18] A.S. Pisat, P.A. Salvador, G.S. Rohrer, The facet structure and photochemical reactivity of arbitrarily oriented strontium titanate surfaces, Adv. Mater. Interfaces 6 (2019), 1900731, https://doi.org/10.1002/admi.201900731.
[19] T. Takata, J. Jiang, Y. Sakata, M. Nakabayashi, N. Shibata, V. Nandal, K. Seki, T. Hisatomi, K. Domen, Photocatalytic water splitting with a quantum efficiency of almost unity, Nature 581 (2020) 411–414, https://doi.org/10.1038/s41586-020-2278-9.
[20] L. Li, P.A. Salvador, G.S. Rohrer, Photocatalysts with internal electric fields, Nanoscale 6 (2014) 24–42, https://doi.org/10.1039/c3nr03998f.
[21] Y. Inoue, M. Okamura, K. Sato, A thin-film semiconducting titanium dioxide combined with ferroelectrics for photoassisted water decomposition, J. Phys. Chem. 89 (1985) 5184–5187, https://doi.org/10.1021/j100270a013.
[22] Y. Inoue, K. Sato, K. Sato, H. Miyama, Photoassisted water decomposition by ferroelectric lead zirconate titanate ceramics with anomalous photovoltaic effects, J. Phys. Chem. 90 (1986) 2809–2810, https://doi.org/10.1021/j100404a006.
[23] S. Dunn, P.M. Jones, D.E. Gallardo, Photochemical growth of silver nanoparticles on c- and c+ domains on lead zirconate titanate thin films, J. Am. Chem. Soc. 129 (2007) 8724–8728, https://doi.org/10.1021/ja071451n.
[24] J.L. Giocondi, G.S. Rohrer, The influence of the dipolar field effect on the photochemical reactivity of $Sr_2Nb_2O_7$ and $BaTiO_3$ microcrystals, Top. Catal. 49 (2008) 18, https://doi.org/10.1007/s11244-008-9067-2.
[25] A.M. Schultz, Y. Zhang, P.A. Salvador, G.S. Rohrer, Effect of crystal and domain orientation on the visible-light photochemical reduction of Ag on $BiFeO_3$, ACS Appl. Mater. Interfaces 3 (2011) 1562–1567, https://doi.org/10.1021/am200127c.
[26] N.V. Burbure, P.A. Salvador, G.S. Rohrer, Photochemical reactivity of titania films on $BaTiO_3$ substrates: influence of titania phase and orientation, Chem. Mater. 22 (2010) 5831–5837, https://doi.org/10.1021/cm1018019.
[27] I. Levin, L.A. Bendersky, Symmetry classification of the layered perovskite-derived $A_nB_nX_{3n+2}$ structures structures, Acta Crystallogr. Sect. B 55 (1999) 853–866, https://doi.org/10.1107/S0108768199005479.
[28] I. Levin, L.A. Bendersky, T.A. Vanderah, A structural study of the layered perovskite-derived $Sr_n(Ti, Nb)_nO_{3n+2}$ compounds by transmission electron microscopy, Philos. Mag. A 80 (2000) 411–445, https://doi.org/10.1080/01418610008212060.
[29] J.K. Yamamoto, A.S. Bhalla, Piezoelectric properties of layered perovskite $A_2Ti_2O_7$ (A=La and Nd) single-crystal fibers, J. Appl. Phys. 70 (1991) 4469–4471, https://doi.org/10.1063/1.349078.
[30] N. Satoshi, K. Masakazu, K. Tsutomu, Crystallographic and dielectric properties of ferroelectric $A_2B_2O_7$ (A=Sr, B=Ta, Nb) crystals and their solid solutions, J. Phys. Soc. Jpn. 38 (1975) 817–824, https://doi.org/10.1143/JPSJ.38.817.

[31] Z.P. Gao, H.X. Yan, H.P. Ning, M.J. Reece, Ferroelectricity of $Pr_2Ti_2O_7$ ceramics with super high Curie point, Adv. Appl. Ceram. 112 (2013) 69–74, https://doi.org/10.1179/1743676112Y.0000000030.
[32] H.G. Kim, D.W. Hwang, J. Kim, Y.G. Kim, J.S. Lee, Highly donor-doped (110) layered perovskite materials as novel photocatalysts for overall water splitting, Chem. Commun. (1999) 1077–1078, https://doi.org/10.1039/a902892g.
[33] D.W. Hwang, H.G. Kim, J.S. Lee, J. Kim, W. Li, S.H. Oh, Photocatalytic hydrogen production from water over M-doped $La_2Ti_2O_7$ (M = Cr, Fe) under visible light irradiation (λ & 420 nm), J. Phys. Chem. B 109 (2005) 2093–2102, https://doi.org/10.1021/jp0493226.
[34] A. Nashim, S. Martha, K.M. Parida, Heterojunction conception of n-$La_2Ti_2O_7$/p-CuO in the limelight of photocatalytic formation of hydrogen under visible light, RSC Adv. 4 (2014) 14633–14643, https://doi.org/10.1039/C3RA47037G.
[35] S.J. Patwe, V. Katari, N.P. Salke, S.K. Deshpande, R. Rao, M.K. Gupta, R. Mittal, S. N. Achary, A.K. Tyagi, Structural and electrical properties of layered perovskite type $Pr_2Ti_2O_7$: experimental and theoretical investigations, J. Mater. Chem. C 3 (2015) 4570–4584, https://doi.org/10.1039/c5tc00242g.
[36] S. Nanamatsu, M. Kimura, K. Doi, S. Matsushita, N. Yamada, New ferroelectric - $La_2Ti_2O_7$, Ferroelectrics 8 (1974) 511–513, https://doi.org/10.1080/00150197408234143.
[37] A. Nashim, K. Parida, n-La2Ti2O_7/p-$LaCrO_3$: a novel heterojunction based composite photocatalyst with enhanced photoactivity towards hydrogen production, J. Mater. Chem. A 2 (2014) 18405–18412, https://doi.org/10.1039/c4ta02401j.
[38] S. Hu, B. Chi, J. Pu, L. Jian, Novel heterojunction photocatalysts based on lanthanum titanate nanosheets and indium oxide nanoparticles with enhanced photocatalytic hydrogen production activity, J. Mater. Chem. A 2 (2014) 19260–19267, https://doi.org/10.1039/C4TA04177A.
[39] F. Meng, Z. Hong, J. Arndt, M. Li, M. Zhi, F. Yang, N. Wu, Visible light photocatalytic activity of nitrogen-doped $La_2Ti_2O_7$ nanosheets originating from band gap narrowing, Nano Res. 5 (2012) 213–221, https://doi.org/10.1007/s12274-012-0201-x.
[40] J.R. Teague, R. Gerson, W.J. James, Dielectric hysteresis in single crystal $BiFeO_3$, Solid State Commun. 8 (1970) 1073–1074.
[41] K. Wenderich, G. Mul, Methods, mechanism, and applications of photodeposition in photocatalysis: a review, Chem. Rev. 116 (2016) 14587–14619, https://doi.org/10.1021/acs.chemrev.6b00327.
[42] P.A. Fuierer, R.E. Newnham, $La_2Ti_2O_7$ ceramics, J. Am. Ceram. Soc. 74 (1991) 2876–2881, https://doi.org/10.1111/j.1151-2916.1991.tb06857.x.
[43] W. Song, P.A. Salvador, G.S. Rohrer, Influence of the magnitude of ferroelectric domain polarization on the photochemical reactivity of $BaTiO_3$, ACS Appl. Mater. Interfaces 10 (2018) 41450–41457, https://doi.org/10.1021/acsami.8b16983.
[44] Z. Shao, S. Saitzek, P. Roussel, A. Ferri, E. Bruyer, A. Sayede, M. Rguiti, O. Mentre, R. Desfeux, Microstructure and nanoscale piezoelectric/ferroelectric properties in $La_2Ti_2O_7$ thin films grown on (110)-oriented doped Nb:$SrTiO_3$ substrates, Adv. Eng. Mater. 13 (2011) 961–969, https://doi.org/10.1002/adem.201100105.
[45] T.C. Kaspar, S. Hong, M.E. Bowden, T. Varga, P. Yan, C. Wang, S.R. Spurgeon, R. B. Comes, P. Ramuhalli, C.H. Henager Jr., Tuning piezoelectric properties through epitaxy of $La_2Ti_2O_7$ and related thin films, Sci. Rep. 8 (2018), https://doi.org/10.1038/s41598-018-21009-5.
[46] D.W. Hwang, J.S. Lee, W. Li, S.H. Oh, electronic band structure and photocatalytic activity of $Ln_2Ti_2O_7$(Ln = La, Pr, Nd), J. Phys. Chem. B 107 (2003) 4963–4970, https://doi.org/10.1021/jp034229n.
[47] E. Bruyer, A. Sayede, Density functional calculations of the structural, electronic, and ferroelectric properties of high-k titanate $Re_2Ti_2O_7$ (Re=La and Nd), J. Appl. Phys. 108 (2010) 53705, https://doi.org/10.1063/1.3459891.
[48] T. Takata, Y. Furumi, K. Shinohara, A. Tanaka, M. Hara, J.N. Kondo, K. Domen, Photocatalytic decomposition of water on spontaneously hydrated layered perovskites, Chem. Mater. 9 (1997) 1063–1064, https://doi.org/10.1021/cm960612b.
[49] X. Cai, M. Zhu, O.A. Elbanna, M. Fujitsuka, S. Kim, L. Mao, J. Zhang, T. Majima, Au nanorod photosensitized $La_2Ti_2O_7$ nanosteps: successive surface heterojunctions boosting visible to near-infrared photocatalytic H_2 evolution, ACS Catal. 8 (2018) 122–131, https://doi.org/10.1021/acscatal.7b02972.
[50] A. Orum, K. Takatori, S. Hori, T. Ikeda, M. Yoshimura, T. Tani, Atomic force microscopy surface analysis of layered perovskite $La_2Ti_2O_7$ particles grown by molten flux method, J. Appl. Phys. 55 (2016), 08NB08, https://doi.org/10.7567/jjap.55.08nb08.
[51] H.M. Tütüncü, G.P. Srivastava, Electronic structure and zone-center phonon modes in multiferroic bulk $BiFeO_3$, J. Appl. Phys. 103 (2008) 83712, https://doi.org/10.1063/1.2908865.
[52] H. Wang, Y. Zheng, M.-Q. Cai, H. Huang, H.L.W. Chan, First-principles study on the electronic and optical properties of $BiFeO_3$, Solid State Commun. 149 (2009) 641–644, https://doi.org/10.1016/j.ssc.2009.01.023.
[53] E. Sagar, R. Mahesh, N. Pavan Kumar, P. Venugopal Reddy, Investigation of structural and multiferroic properties of three phases of $BiFeO_3$ using modified Becke Johnson potential technique, J. Phys. Chem. Solids 110 (2017) 316–326, https://doi.org/10.1016/j.jpcs.2017.06.023.
[54] N.G. Apostol, L.E. Stoflea, G.A. Lungu, C.A. Tache, D.G. Popescu, L. Pintilie, C. M. Teodorescu, Band bending at free Pb(Zr,Ti)O_3 surfaces analyzed by X-ray photoelectron spectroscopy, Mater. Sci. Eng. B 178 (2013) 1317–1322, https://doi.org/10.1016/j.mseb.2013.02.007.
[55] A. Höfer, M. Fechner, K. Duncker, M. Hölzer, I. Mertig, W. Widdra, Persistence of surface domain structures for a bulk ferroelectric above TC, Phys. Rev. Lett. 108 (2012) 87602, https://doi.org/10.1103/PhysRevLett.108.087602.
[56] M.R. Morris, S.R. Pendlebury, J. Hong, S. Dunn, J.R. Durrant, Effect of internal electric fields on charge carrier dynamics in a ferroelectric material for solar energy conversion, Adv. Mater. 28 (2016) 7123–7128, https://doi.org/10.1002/adma.201601238.

Supporting materials for:

Influence of Orientation and Ferroelectric Domains on the Photochemical Reactivity of $La_2Ti_2O_7$

Mingyi Zhang, Paul A. Salvador, Gregory S. Rohrer*

Department of Materials Science and Engineering, Carnegie Mellon University, Pittsburgh PA 15213 USA

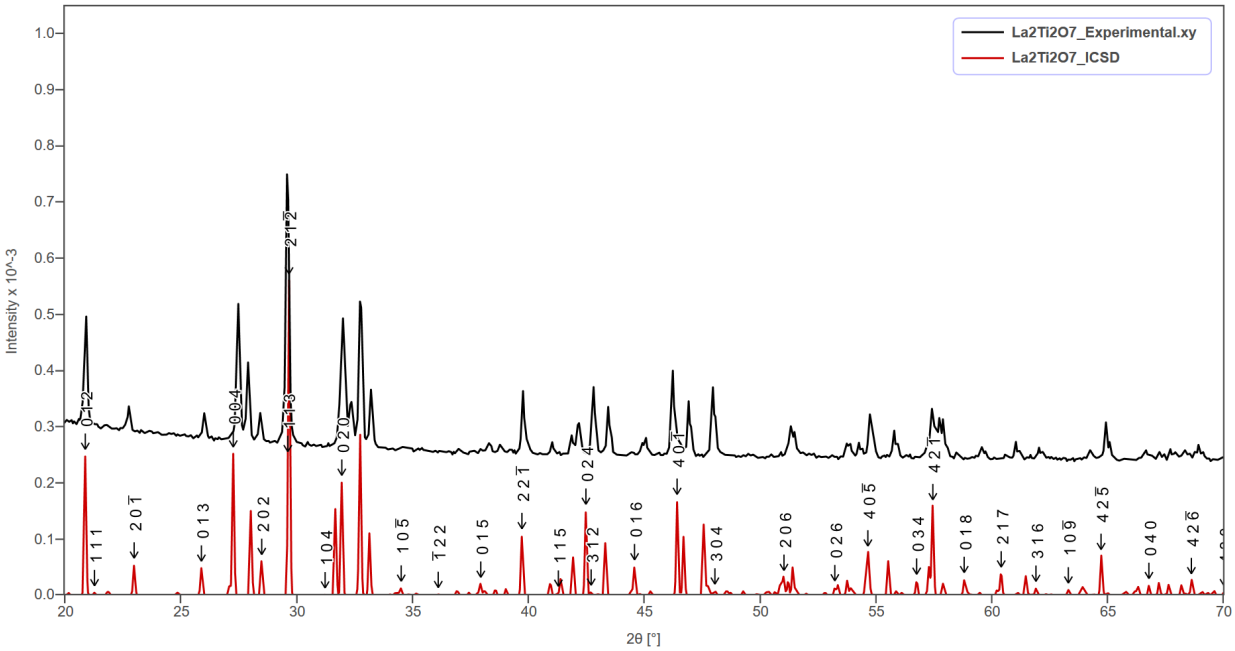

Figure S1: Black line corresponds to the XRD pattern of the $La_2Ti_2O_7$ powder synthesized with molten salt method in this work. Red line corresponds to a calculated pattern of the $La_2Ti_2O_7$. (ICSD IDs: 5416 1950)

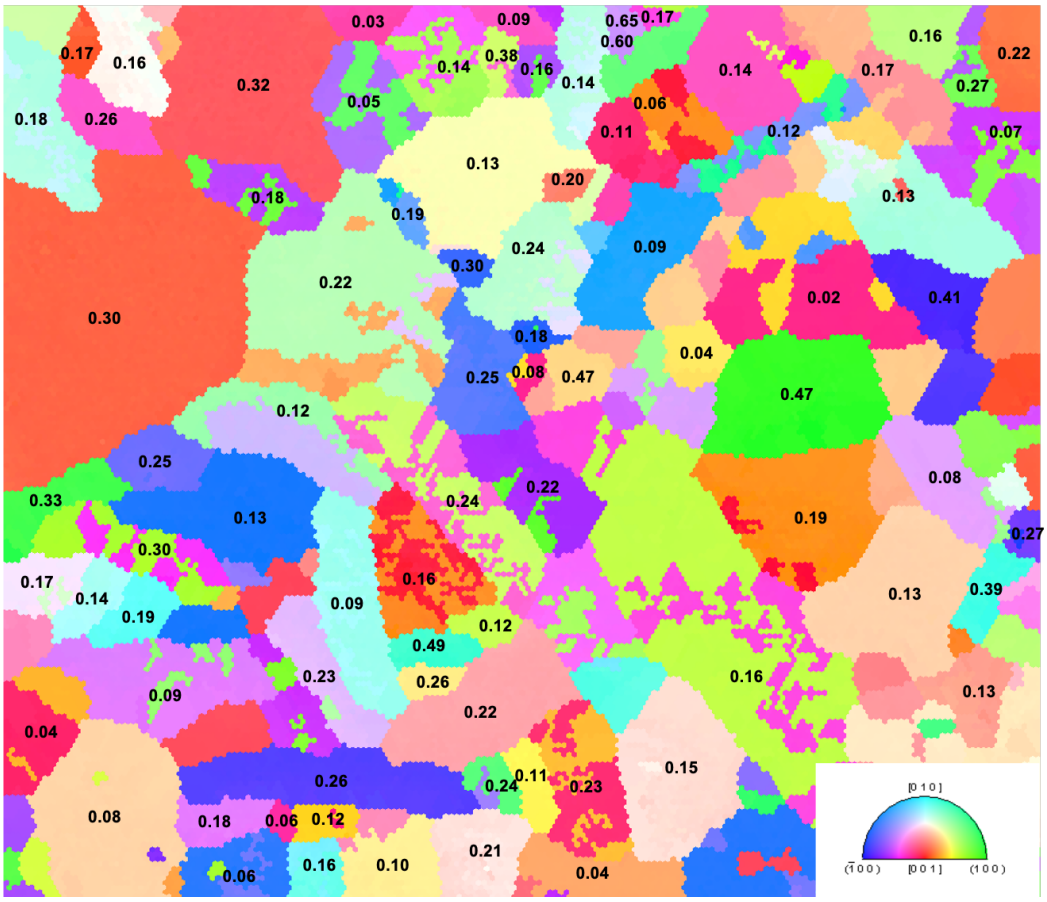

Figure S2: An orientation map for the same location shown in Figure 1(b), with the confidence index (CI) assigned by the OIM Analysis Software labelled on most grains.

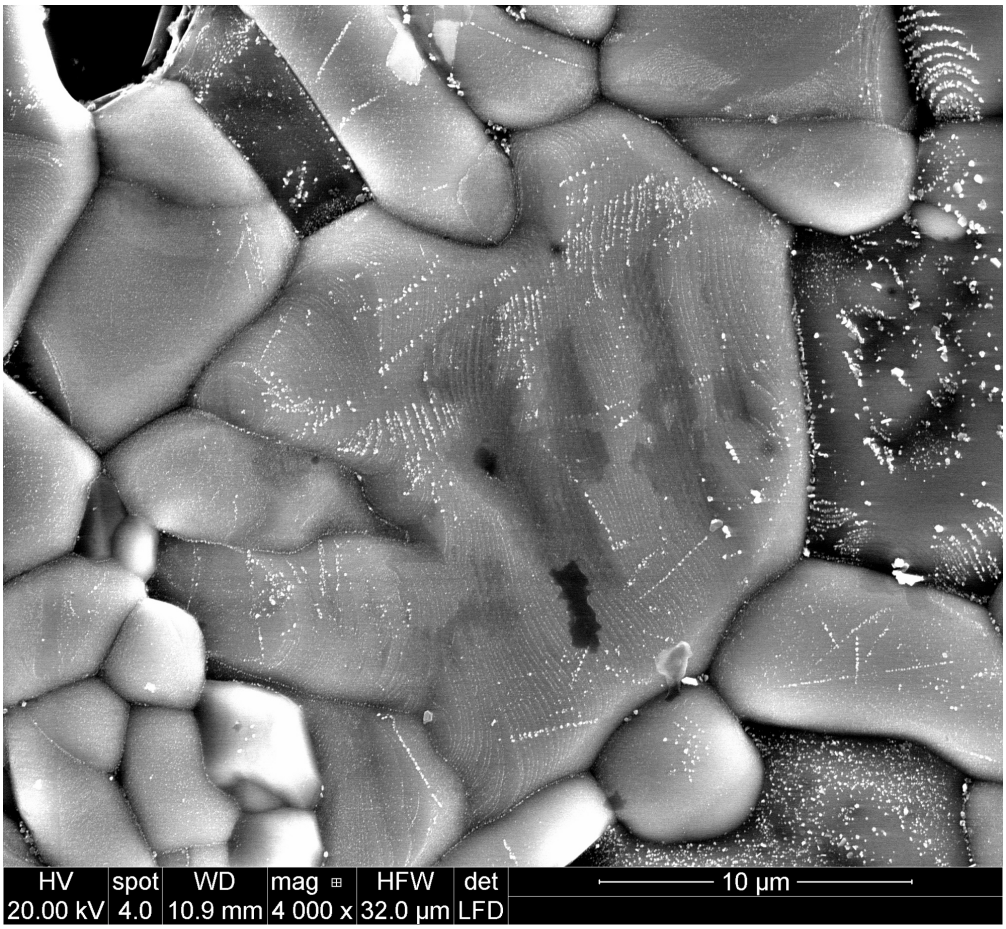

Figure S3: A higher resolution SEM image after reaction for the large grain labeled “H” at left top of Figure 1(a), which is “near red” (near (001)) in Figure 1(b).

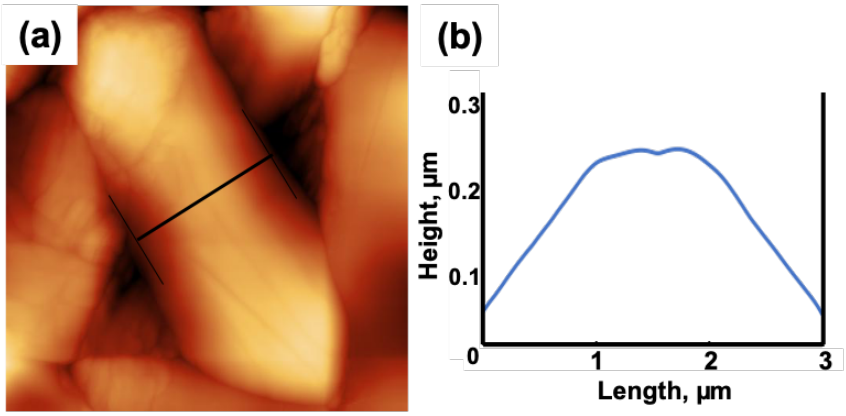

Figure S4. (a) Topographic AFM image recorded in contact mode, showing the same field of view as the images in Figure 6(c) and (d). The dark-to-white contrast shown is 500 nm. (b) Height profile extracted from the line dawn in (a).

Figure S5 shows images of a grain (running from top left to bottom right through the center of all images) whose orientation is inclined by about 48° from the polar [010] axis. Figures S5(a) and S5(b) are SE images showing the surface before and after the photochemical reduction of silver, respectively. Figures S5(c) and S5(d) are PFM out-of-plane images, respectively of the amplitude and phase, of the same grain. Similar to the results shown in Figure 6, silver did not deposit uniformly and there is no correlation between silver pattern and PFM pattern. Note that there is an artifact in the PFM image where the complex shape of the domain is repeated; this results from the sloped surface, which sometimes causes the image to be formed from different areas of the tip.

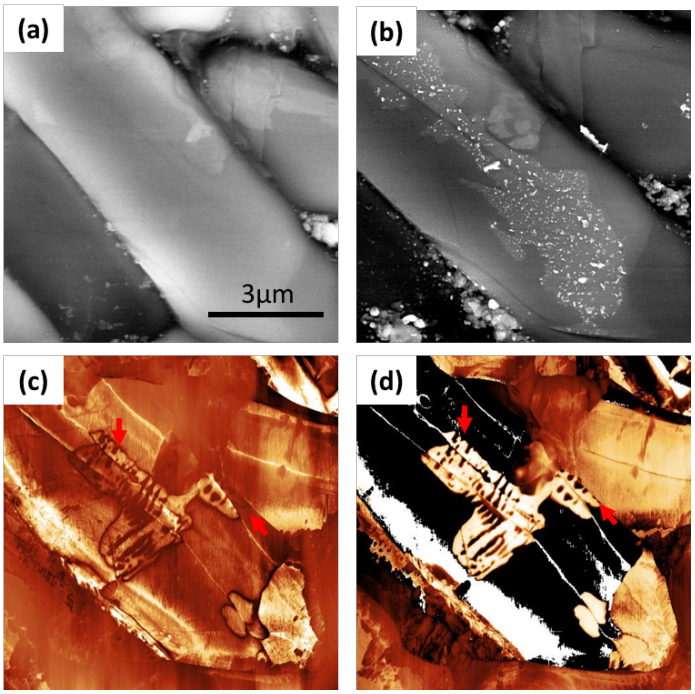

Figure S5: (a) an SEM image before reaction. (b) an SEM image of the same grain after silver reduction. (c) a PFM out-of-plane amplitude image of the same grain. (d) a PFM out-of-plane phase image of the same grain. Darker regions correspond to domains with positive polarizations, and brighter regions correspond to domains with negative polarizations. Arrows in (c) and (d) mark artifacts caused by a tip issue (see text).

In this work, in order to illustrate the distribution of the two types of reactivity more directly, the angle of inclination of the grains from [001] was classified in bins 10° wide and the fraction of grains in each bin was assigned a population in units of multiples of a random distribution (MRD). MRD quantifies the ratio of the number of grains in a given bin to the number that would be if there is a random distribution.

Table S1: Details of population analysis in Fig. 5.

	Total Grains (#)	**Random Population**	**High Reactivity (#)**	**High Reactivity (MRD)**	**Low Reactivity (#)**	**Low Reactivity (MRD)**
0°~10°	2	0.015298	2	2.66808	0	0
10°~20°	5	0.044812	5	2.27707	0	0
20°~30°	6	0.073812	6	1.65893	0	0
30°~40°	8	0.10015	7	1.42643	1	0.23221
40°~50°	13	0.12384	8	1.31835	5	0.93895
50°~60°	10	0.14309	7	0.99837	3	0.48758
60°~70°	21	0.15710	10	1.29906	11	1.62835
70°~80°	10	0.16841	0	0	10	1.3809
80°~90+°	17	0.17349	4	0.47053	13	1.74261